Intermediate mass fragment emission in ^{36}Ar$+^{197}$Au collisions at $E/A = 35$ MeV

Y. D. Kim,* R. T. de Souza,† D. R. Bowman, N. Carlin,‡ C. K. Gelbke, W. G. Gong,§
W. G. Lynch, L. Phair, M. B. Tsang, and F. Zhu
*National Superconducting Cyclotron Laboratory and Department of Physics and Astronomy,
Michigan State University, East Lansing, Michigan 48824*
(Received 14 June 1991)

Intermediate mass fragment (IMF: $3 \leq Z \leq 20$) emission for the ^{36}Ar$+^{197}$Au reaction at $E/A = 35$ MeV has been studied with a low-threshold 4π charged-particle detector array covering the angular range of $16° \leq \theta_{lab} \leq 160°$. While most IMF's are emitted in central collisions characterized by large charged-particle multiplicities, contributions from peripheral collisions exist at forward angles which are reminiscent of damped collisions or emission from a projectile-like source. Energy spectra, angular distributions, element distributions, and two-fragment correlation functions are presented for various gates on the charged-particle multiplicity, and the time scale of fragment emission is deduced.

I. INTRODUCTION

Highly excited nuclear matter can be produced in intermediate-energy nucleus-nucleus collisions. As the excitation energy is raised from below 1 MeV per nucleon up to about 10 MeV per nucleon, decay of the excited nuclear matter by intermediate mass fragment (IMF: $3 \leq Z \leq 20$) emission is both predicted and observed to become a significant deexcitation channel [1–58]. The production of multifragment final states may be related to thermodynamic instabilities or dynamical effects. The nuclear system can expand in response to the action of thermal pressure [1–4,38,40] or to a dynamical compression-decompression cycle resulting from the collision dynamics [1,5–13]. If it expands to sufficiently low densities, nuclear matter becomes unstable and density fluctuations can grow exponentially as a function of time [1], possibly yielding a multifragment [5–13] final state. Calculations suggest that the probability for multifragment breakup may be sensitive to the nuclear equation of state at low density [14]. Therefore, information about the low-density equation of state and the liquid-gas phase transition of nuclear matter may be obtainable from detailed studies of multifragment emission processes [5–7,9,15–17,44–46]. Alternatively, semiclassical simulations of the reaction dynamics suggest that multifragment decays could reflect dynamical fluctuations rather than thermodynamic instabilities and could thus yield information about the collision dynamics [18].

At present, a full theoretical understanding of multifragment production processes in finite nuclear systems

is not available and alternative models for multifragment emission have been proposed, ranging from static thermodynamical treatments [19–34] to rate-equation approaches based on generalizations of compound-nucleus decay models [35–42]. Additional experimental information is clearly necessary to discriminate between the various theories. Essential to distinguishing between these different theories is the time scale of the multifragment process. Two-particle correlations at small relative momenta offer the opportunity to probe the space-time evolution of excited nuclear systems [59–72].

As part of a systematic study of reactions in which multifragment final states are produced, we have investigated the ^{36}Ar$+^{197}$Au reaction at the incident energy of $E/A = 35$ MeV using a low-threshold 4π charged-particle detection system [73]. In this paper we present charged-particle and IMF multiplicity distributions, elemental distributions, energy spectra, angular distributions, and two-fragment correlation functions measured at small relative momenta. The nonequilibrium nature of the energy spectra is discussed. Fragment emission arising from both peripheral and central collisions will be studied. Previous results on two-fragment correlations [71] will be explored in greater detail.

Experimental details are given in Sec. II. General features of the reaction, charged-particle and intermediate mass fragment multiplicity distributions, measured IMF element distributions, representative energy spectra, and angular distributions, are presented in Sec. III. Two-fragment correlation functions are extracted and discussed in Sec. IV. Section V contains the summary and conclusions.

*Present address: Indiana University Cyclotron Facility, Indiana University, Bloomington, IN 47405.

†Present address: Department of Chemistry and Indiana University Cyclotron Facility, Indiana University, Bloomington, IN 47405.

‡Present address: Instituto de Fisica, Universidade de São Paulo, C. Postal 20516, CEP 01498, São Paulo, Brazil.

§Present address: Lawrence Berkeley Laboratories, University of California, Berkeley, CA 94720.

II. EXPERIMENTAL DETAILS

The experiment was performed in the 92 in.-diam scattering chamber of the National Superconducting Cyclotron Laboratory at Michigan State University (MSU). An ^{36}Ar beam of energy $E/A = 35$ MeV and intensity $I \approx 10^8$ particles per second was extracted from the K500 cyclotron. Typical beam spot diameters were of the order of 2–3 mm. The target foil consisted of 1 mg/cm^2

^{197}Au. During the experiment, a vacuum of better than 10^{-5} torr was maintained in the scattering chamber. Water and hydrocarbon vapor components in the residual gas were strongly reduced by a large cold trap filled with liquid nitrogen. By this means carbon deposits on the target were reduced to a negligible level, eliminating contamination from auxiliary reactions.

Light particles and complex fragments were detected using rings 2–11 of the MSU Miniball phoswich detector array [73]. In this configuration the array covered scattering angles of $\theta_{lab} = 16° - 160°$ and subtended a solid angle corresponding to 85% of 4π. In Table I the solid angles and ranges of polar and azimuthal angles covered by individual detectors of the Miniball are listed. The geometrical shapes of the detectors are described in Ref. [73]. As a precaution against secondary electrons, rings 2 and 3 were covered by aluminum foils of 0.81 mg/cm^2 areal density. The detector array was actively cooled, and its temperature was stabilized. Gain drifts of the photomultiplier tubes were monitored by a light pulser system [73]. Most data were taken with a hardware trigger of $N_{hit} \geq 2$, where N_{hit} denotes the number of detectors firing; a run with reduced statistics was taken with $N_{hit} \geq 1$. Details about the electronics and data-acquisition system are described at greater length in Ref. [73].

Particles which penetrated the 4-mg/cm^2 plastic scintillator foils and entered the CsI(Tl) crystals were identified by atomic number up to $Z \approx 20$. In addition, the isotopes of H and He were identified. Approximate energy thresholds are $E_{th}/A \approx 2$ MeV for $Z=3$, $E_{th}/A \approx 3$ MeV for $Z=10$, and $E_{th}/A \approx 4$ MeV for $Z=18$ fragments. Particles of lower energy which stopped in the scintillator foils were recorded, but could not be identified by atomic number. All events in which at least two detectors fired were recorded on magnetic tape and analyzed off line. Because of the low beam intensity, random coincidences were negligible.

Energy calibrations, accurate to within 5%, were obtained by measuring the elastic scattering of ^{4}He, ^{6}Li, ^{10}B, ^{12}C, ^{16}O, and ^{35}Cl beams from a ^{197}Au target at incident energies of $E(^4$He$/A=4.5$, 9.4, 12.9, 16, and 20 MeV; $E(^6$Li$)/A=8.9$ MeV; $E(^{10}$B$)/A=15$ MeV; $E(^{12}$C$)/A=6$, 8, 13, and 20 MeV; $E(^{16}$O$)/A=6$, 8, 16, and 20 MeV; and $E(^{35}$Cl$)/A=8.8$, 12.3, and 15 MeV.

TABLE I. Coverage in solid, polar, and azimuthal angles for individual detectors of the Miniball. Ring 1 was not used in this experiment.

Ring	θ (deg)	$\Delta\Omega$ (msr)	$\Delta\theta$ (deg)	$\Delta\phi$ (deg)
1	12.5	12.3	7	30
2	19.5	14.7	7	22.5
3	27.0	18.5	8	18.0
4	35.5	22.9	9	15.0
5	45.0	30.8	10	15.0
6	57.5	64.8	15	18.0
7	72.5	74.0	15	18.0
8	90.0	113.3	20	20.0
9	110.0	135.1	20	25.7
10	130.0	128.3	20	30.0
11	150.0	125.7	20	45.0

III. GENERAL REACTION CHARACTERISTICS

A qualitative perspective of the reaction is depicted by the multiplicity distribution of identified charged particles in Fig. 1. The threshold at $N_C = 2$ is due to the hardware trigger employed during most of the experiment. To a rough approximation, the charged-particle multiplicity is determined by the deposition of energy from relative motion into internal degrees of freedom. Within a simple geometric picture of the collision, this energy deposition depends on the impact parameter of the collision—more central collisions being associated with greater energy deposition and hence larger charged-particle multiplicities. At higher bombarding energies [74], cuts on the charged-particle multiplicity are commonly used for the selection of different impact parameter ranges. While a purely geometric interpretation of the measured charged-particle multiplicities may not be strictly applicable at this low energy, it can nevertheless be utilized to generate a rough impact parameter scale. In the bottom part of Fig. 1, such a scale is constructed by using the geometric prescription of Ref. [74] in which a monotonic relation between the charged-particle multiplicity and impact parameter is assumed:

$$(b/b_{max})^2 = \int_{N_C}^{\infty} [dP(N_C')/dN_C']dN_C' . \qquad (1)$$

Here $dP(N_C)/dN_C$ is the normalized probability distribution for the measured charged-particle multiplicity and b_{max} is the maximum parameter for which particles were detected in the Miniball ($N_C \geq 1$). This relative scale between impact parameter and charged-particle multiplicity must not be overinterpreted since considerable fluctuations of the charged-particle multiplicity must be expected even for collisions of well-defined impact parameter. Nevertheless, it appears reasonable to distinguish be-
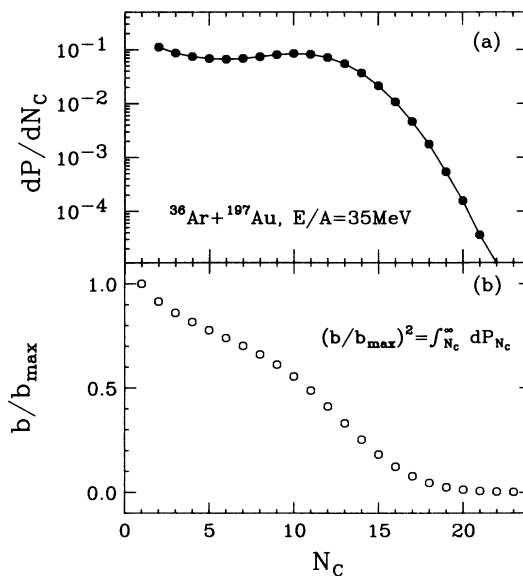

FIG. 1. (a) Multiplicity distribution of identified charged particles detected in this experiment; consistent with the hardware trigger of $N_{hit} \geq 2$, a software cut of $N_C \geq 2$ was applied. (b) Relation between charged-particle multiplicity and impact parameter obtained from the geometrical prescription of Ref. [74].

tween "central," "midcentral," and "peripheral" collisions by applying multiplicity cuts corresponding to $N_C \geq 12$, $8 \leq N_C \leq 11$, and $2 \leq N_C \leq 7$, respectively. Events with $N_C = 1$ were not included in this definition of peripheral collisions.

Experimental multiplicity distributions for intermediate mass fragments detected in peripheral, midcentral, and central collisions are shown in Fig. 2. The Poisson-like shape of the IMF distribution has been reported earlier [57]. For peripheral collisions the IMF multiplicity distribution is peaked at $N_{IMF} = 0$, indicating that IMF emission is an improbable outcome. For midcentral collisions the peak of the IMF multiplicity distribution is at $N_{IMF} = 1$. For these collisions IMF emission is a common process and multiple IMF emission occurs fairly frequently. For central collisions the IMF multiplicity distribution does not change dramatically from the midcentral distribution. For central collisions the IMF distribution is still peaked at $N_{IMF} = 1$, except that the probabilities for multiple IMF emission ($N_{IMF} = 3-7$) are increased in probability by a factor of 2-10.

The dependence of the mean IMF multiplicity $\langle N_{IMF} \rangle$ on the charged-particle multiplicity N_C is depicted in Fig. 3. Over a broad range of charged-particle multiplicities N_C, the mean IMF multiplicity $\langle N_{IMF} \rangle$ exhibits an approximately linear rise as a function of N_C. For very high multiplicities, $N_C \gtrsim 12$, the mean IMF multiplicity levels off as a function of N_C and reaches an asymptotic value of $\langle N_{IMF} \rangle \approx 1.2$. To determine whether this behavior is dominated by the inclusion of Li fragments in our definition of IMF, we have explored the dependence of the mean IMF multiplicity $\langle N_{IMF} \rangle$ on the charged-particle multiplicity N_C when an IMF is redefined to exclude Li fragments ($4 \leq Z \leq 20$). Qualitatively, the dependence of the mean IMF multiplicity on charged-particle multiplicity is the same, irrespective of the inclusion of Li fragments in the definition of IMF's.

The relationship between the IMF and total charged-particle multiplicities can be qualitatively understood by assuming that the charged-particle multiplicity is strongly correlated with energy deposition and that the production of intermediate mass fragments depends primarily upon this energy deposition. The observed increase of $\langle N_{IMF} \rangle$ as a function of N_C can thus be viewed as due to the selection of interactions involving progressively increasing amounts of internal energy deposition. In the extreme tails of the N_C distributions, however, the correlation between internal energy and N_C becomes dominated by fluctuations of the charged-particle multiplicity. Hence very large values of N_C become ineffective in selecting nuclei of increasing internal energy, thus causing the observed saturation of $\langle N_{IMF} \rangle$ at large values of N_C. This loss of selectivity for $N_C \gtrsim 12$ is also expected from the impact parameter scale provided in Fig. 1(b).

In order to explore whether intermediate mass fragments provide impact parameter selectivity, we investigated the dependence of the charged-particle multiplicity distribution on the IMF multiplicity and detection angle of the IMF. The left-hand panel of Fig. 4 shows the correlation between IMF multiplicity and associated charged-particle multiplicity. Such a relationship has been investigated previously [57] for reactions contributing to the fission channel. While larger charged-particle multiplicities are measured in the present experiment, qualitatively similar trends are observed as reported in Ref. [57]. Events without an IMF are dominated by peripheral (low charged-particle multiplicity) reactions. Requirement of one intermediate mass fragment substantially suppresses contributions from peripheral processes. The dependence of the charged-particle multiplicity on the detection angle of the IMF is shown in the right-hand
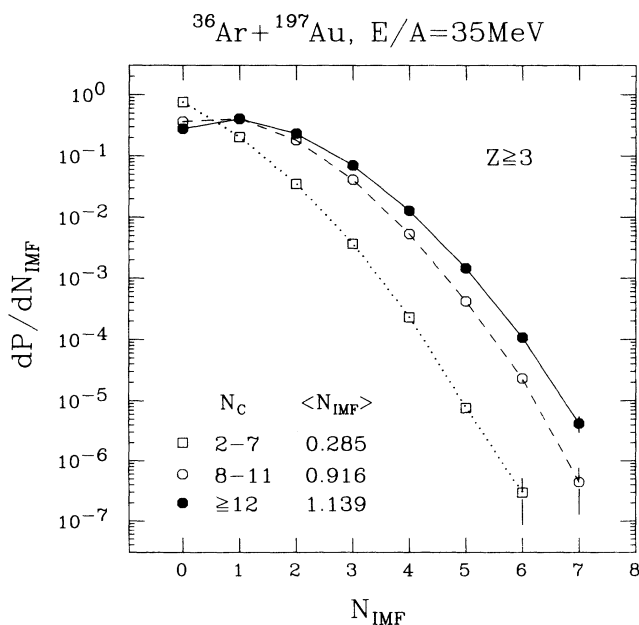

FIG. 2. Normalized conditional probability distributions dP/dN_{IMF} of detecting N_{IMF} intermediate mass fragments in collisions preselected by the indicated gates on charged-particle multiplicity N_C. Mean values $\langle N_{IMF} \rangle$ are given in the figure.
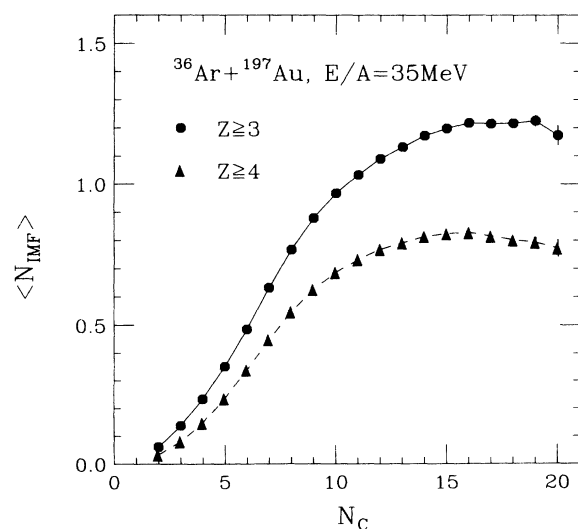
FIG. 3. Mean IMF multiplicity $\langle N_{IMF} \rangle$ (circular points) as a function of the charged-particle multiplicity N_C. Triangular points show mean multiplicities when lithium nuclei are excluded from the definition of IMF's.
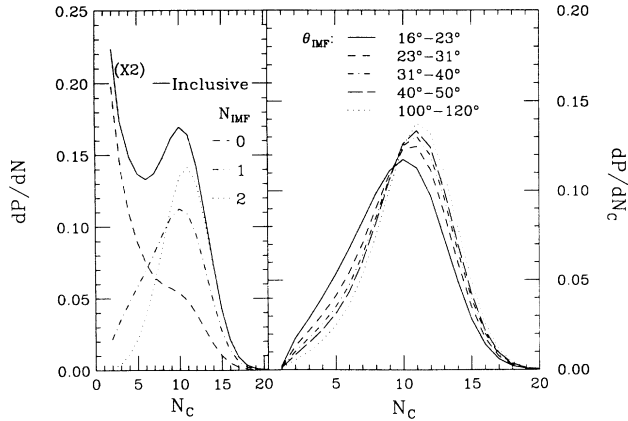
FIG. 4. Charged-particle multiplicity distributions dP/dN_C measured for collisions preselected by the detection of $N_{IMF}=0$, 1, and 2 intermediate mass fragments at any angle (left-hand panel) and by the detection of a fragment at a given angle (right-hand panel).

panel of Fig. 4. In all cases IMF emission selects violent collisions characterized by large charged-particle multiplicities. While a slight shift in the charged-particle multiplicity distribution to lower multiplicities is observed when fragments are detected at $16° \leq \theta_{lab} \leq 23°$, the angular sensitivity of the charged-particle multiplicity distributions to the fragment detection angle is insignificant at larger angles.

Examples of elemental distributions, integrated over the angular range of $16° \leq \theta_{lab} \leq 120°$, are shown in Fig. 5. Solid points show the inclusive $(N_C \geq 2)$ distributions;
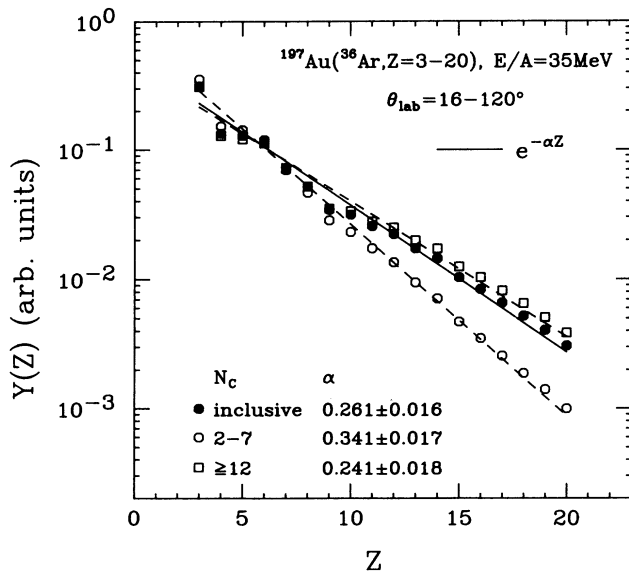

FIG. 5. Comparison of angle integrated element distributions measured inclusively (solid points), in central collisions ($N_C \geq 12$, open squares) and in peripheral collisions ($2 \leq N_C \leq 7$, open circles). The lines represent parametrizations with exponential functions; ranges of parameters consistent with charge distributions are indicated.

open squares and open circles show distributions measured for the peripheral $(2 \leq N_C \leq 7)$ and central $(N_C \geq 12)$ gates on charged-particle multiplicity, respectively. (To facilitate the comparison of relative shapes, the distributions were renormalized.) All three elemental distributions exhibit near exponential shapes. Examples of fits with exponential functions $e^{-\alpha Z}$ are shown by the solid and dashed curves for the parameters given in the figure; the indicated errors are estimates of the systematic uncertainties arising from the fact that the elemental distributions do not strictly follow exponential shapes. The elemental distribution measured for the peripheral gate exhibits a slightly steeper slope than that measured for the central gate. However, the inclusive distribution is very similar in shape to that observed in central collisions. This similarity is related to the fact that IMF emission is strongly suppressed for peripheral collisions, which, hence, make only minor contributions to the inclusive cross section. Inclusive mass or charge distributions may not always be quite as meaningless as suggested previously [10–12].

The parameters α describing elemental distributions gated by different IMF multiplicities are shown in the left-hand panel of Fig. 6. While the shapes of the elemental distributions are not very sensitive to the IMF multiplicity, there is a discernible trend for the elemental distributions to become slightly steeper as more fragments are emitted.

We cannot offer a quantitative explanation of the dependence of α on N_C. However, some of the qualitative trends are consistent with statistical considerations. Within a statistical picture of fragment emission, the slope of the charge distribution is expected to become less steep when the temperature of the emitting system is raised and Coulomb barrier effects are reduced. As increasing values of N_C are related to higher internal energies of the emitting system, the qualitative trend of reduced slopes in the elemental distributions is expected. However, the increase at very large values of N_C is not
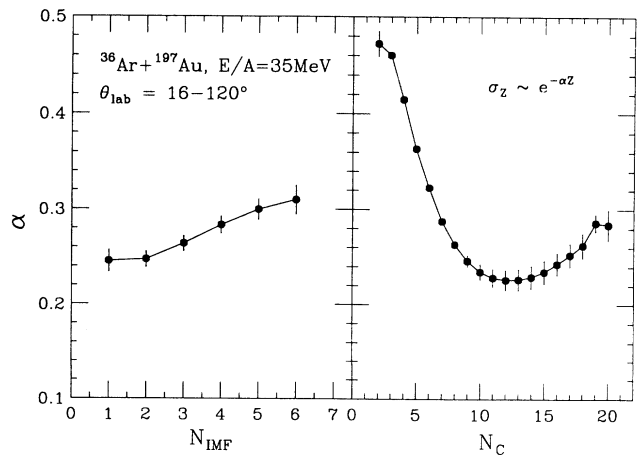

FIG. 6. Parameters of exponential $(e^{-\alpha Z})$ fits to element distributions selected by cuts on N_{IMF} (left-hand panel) and N_C (right-hand panel).

Y. D. KIM *et al.*

expected, and its origin remains less clear. It could be related to self-correlations imposed by energy conservation. Gates on the extreme tails of the charged-particle multiplicity distribution select events in which statistical fluctuations have lead to the emission of more charged particles than average. If intermediate mass fragments are emitted at the later stages of the reaction, the fragment emitting system will then have a slightly reduced excitation energy, and the slope of the resulting fragment distribution should be slightly steeper.

Examples of inclusive energy spectra are presented in Fig. 7 for intermediate mass fragments of charge $Z=4-9$. The energy spectra exhibit qualitative characteristics already observed in other heavy-ion-induced reactions at comparable energies [43,49–52,75]. In order to provide a reasonable analytic parametrization of these cross sections, we have fitted them with a simple parametrization, allowing for contributions from three sources of different velocities. Each source was assumed to emit particles with a $1/\sin\theta$ angular distribution in its respective rest frame. The explicit form of the adopted parametrization is taken from Ref. [76]:

$$\frac{d^2P}{dE\,d\Omega} = \sum_{i=1}^{n} N_i(\sqrt{E_{si}}/\sin\theta)\exp(-E_{si}/T_i) , \quad (2)$$

where

$$E_{si} = E - V_C + E_i - 2\sqrt{E_i(E - V_C)}\cos\theta \quad (3)$$

and

$$E_i = \tfrac{1}{2}mv_i^2 . \quad (4)$$

Here T_i is a kinetic temperature parameter characterizing the slope of the energy spectrum for the ith source and v_i is the source velocity. The parameter V_C is introduced to account for Coulomb repulsion from a heavy charge assumed, for simplicity, at rest in the laboratory system. To simulate the kinematics of fragment emission from equilibrated residues formed in an incomplete fusion reaction, the velocity of one source was fixed at $v_2=0.035c$. This value corresponds to a linear momentum transfer of 80%, consistent with the systematics of Refs. [77,78]. The fits are shown by the solid curves in Fig. 7, and the parameters are listed in Table II. The fitted parameters may not be unique, since they depend on the specific parametrization adopted and, in addition, on the energy and angular range included in the fit [75]. Nevertheless, the fits strongly suggest contributions from fusionlike and projectilelike sources ($i=2$ and 3, respectively) as well as from an intermediate velocity source ($i=1$) representing nonequilibrium processes.

Rather large differences are observed in the shapes of energy spectra gated by different ranges of impact parameters. For illustration, Fig. 8 presents the energy distributions measured for carbon fragments produced in peripheral ($2 \le N_C \le 7$, sold circular points), midcentral ($8 \le N_C \le 11$, open points), and central ($N_C \ge 12$, solid triangular points) collisions. As before, the distributions represent conditional probability distributions per unit energy and solid angle for detecting a given fragment in collisions preselected by the indicated gate on N_C. Consistent with Fig. 2, the fragment emission probabilities are smaller in magnitude for peripheral than for central
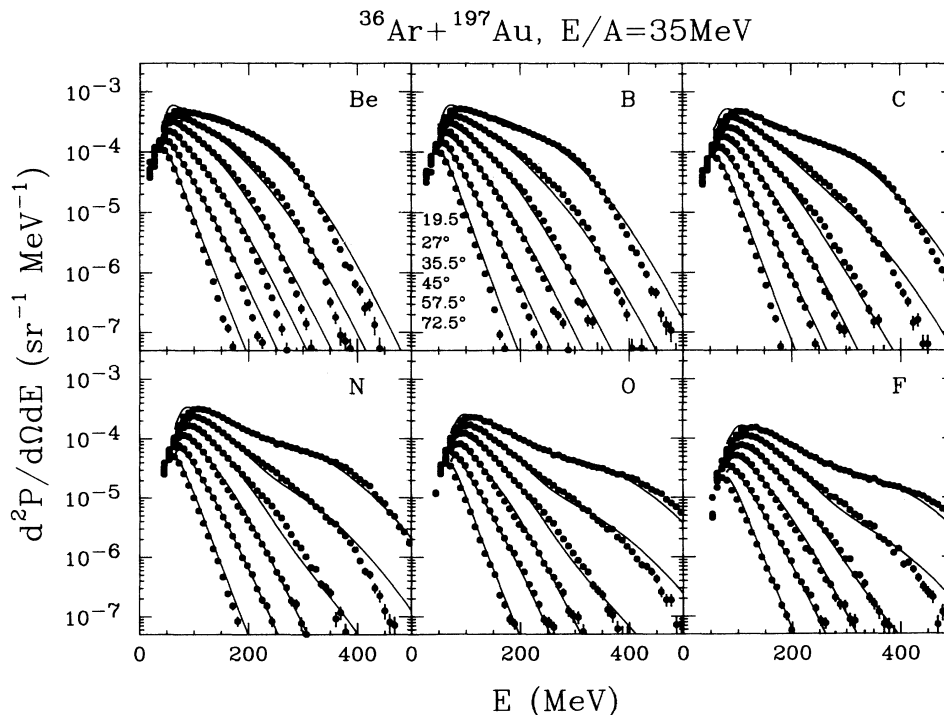

^{36}Ar$+^{197}$Au, E/A=35MeV

FIG. 7. Inclusive energy spectra for intermediate mass fragments of charge $Z=4-9$. The curves represent moving source fits [Eq. (2)] with the parameters given in Table II.

TABLE II. Parameters of three-source fits [Eq. (3), using $n = 3$] to inclusive fragment spectra. The normalization constants N_i are given in units of $10^{-4}/\text{sr}\,\text{MeV}^{3/2}$.

Z	N_1	v_1/c	T_1 (MeV)	N_2	v_2/c	T_2 (MeV)	N_3	v_3/c	T_3 (MeV)
4	0.748	0.107	15.3	0.516	0.035	11.4	0.734	0.196	9.2
5	0.793	0.108	14.8	0.526	0.035	11.4	0.896	0.200	9.4
6	0.712	0.096	14.9	0.378	0.035	12.6	0.739	0.194	10.4
7	0.521	0.085	14.1	0.223	0.035	9.9	0.375	0.183	11.8
8	0.349	0.078	14.1	0.231	0.035	8.8	0.223	0.170	12.6
9	0.231	0.078	14.8	0.123	0.035	10.6	0.148	0.170	12.3

collisions. For central collisions the energy spectra exhibit rather featureless exponential slopes, which become steeper at larger emission angles. For peripheral collisions the energy spectrum at $\theta_{\text{lab}} = 19.5°$ exhibits a large high-energy shoulder, indicating possible contributions from the decay of projectilelike residues or from strongly damped collisions. Midcentral collisions exhibit an intermediate behavior. At larger angles this shoulder vanishes, and the energy spectra attain structureless exponential shapes. However, the slopes of the energy spectra observed in peripheral collisions are less steep than the slopes of the energy spectra measured for central collisions.

The exponential shapes of the energy spectra observed in central collisions suggest emission from a system characterized by a relatively high degree of equilibration. In order to explore whether fragment production in central collisions is consistent with emission from fully

$$^{197}\text{Au} \; (^{36}\text{Ar,C}), \; E/A = 35\text{MeV}$$

FIG. 8. Energy distributions of carbon fragments produced in peripheral ($2 \le N_C \le 7$, solid circular points), midcentral ($8 \le N_C \le 11$, open points), and central ($N_C \ge 12$, solid triangular points) collisions. The fragment detection angles are indicated in the individual panels. The distributions represent conditional probability distributions per unit energy and solid angle for detecting a given fragment in collisions preselected by the indicated gate on N_C.

equilibrated reaction residues formed in fusionlike processes, we have fitted the differential emission probabilities with a two-source parametrization, allowing for contributions from a fusionlike source and an intermediate velocity source, each parametrized according to Eqs. (2)–(4) (using $n = 2$). Figure 9 shows energy spectra and two-source fits for fragments with $4 \le Z \le 9$ observed in central collisions ($N_C \ge 12$); parameters are listed in Table III. The fits indicate significant contributions from nonequilibrium emission processes.

Angular distributions of representative intermediate mass fragments, gated by peripheral ($2 \le N_C \le 7$, open circular points) and central ($N_C \ge 12$, open square-shaped points) collisions, are shown in Fig. 10. For comparison, inclusive angular distributions are depicted by solid points. The angular distributions shown in the figure are normalized as conditional probability distributions, i.e., as the probability per unit solid angle to detect a given fragment in collisions preselected by the indicated gate on charged-particle multiplicity. In general, the angular distributions become more forward peaked for increasing fragment charge. The slopes of the angular distributions are steeper for peripheral collisions than for central collisions, which could indicate increasing degrees of equilibration and possibly diminishing contributions from projectilelike sources for collisions with larger charged-particle multiplicities.

To give an overall qualitative perspective of the ratio of equilibrium to nonequilibrium emission in central collisions, we show in Fig. 11 the equilibrium fraction, $\sigma_{\text{slow}}/\sigma_{\text{total}}$, indicated by the fits in Fig. 9. Here σ_{slow} represents the cross section represented by the slow fusionlike source ($i = 2$) and σ_{total} represents the summed cross section from the two sources ($i = 1 + 2$). The top panel depicts the equilibrium fraction as a function of laboratory angle with the individual source contributions integrated over the energy spectrum above the detection threshold. The bottom panel shows this fraction as a function of fragment momentum per nucleon with the individual source contributions integrated over the angular range of $16° \le \theta_{\text{lab}} \le 31°$. While the decomposition into equilibrium and nonequilibrium processes may not be unique, the extracted ratios should, nevertheless, provide a qualitative estimate of the fraction which may be emitted by an equilibrated heavy residue. Nonequilibrium contributions are most important at forward angles and for fragments emitted with high kinetic energy. At larger angles the fragment cross sections are increasingly consistent with emission from equilibrium decays.
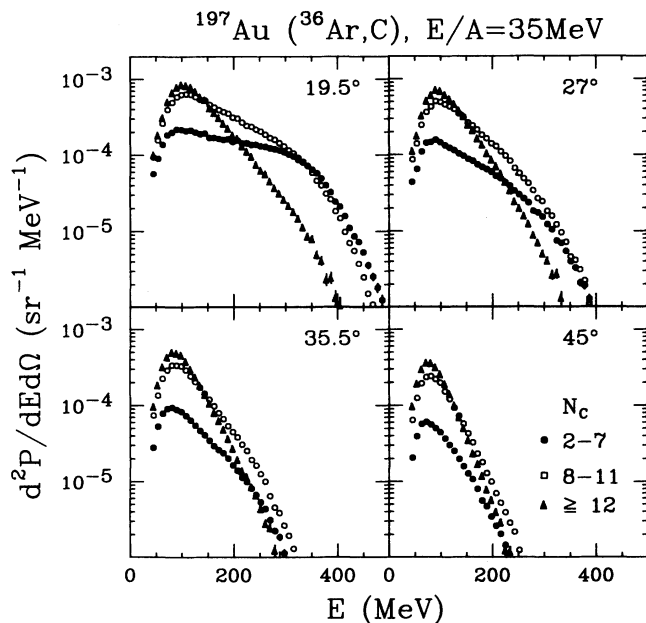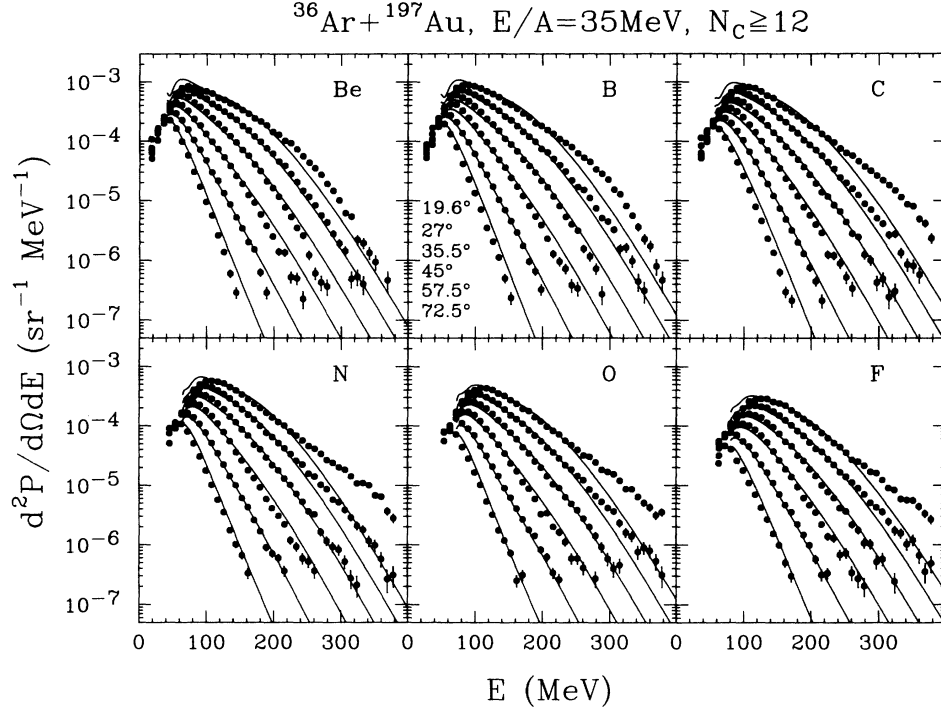
$$^{36}\mathrm{Ar} + {}^{197}\mathrm{Au}, \quad E/A = 35\mathrm{MeV}, \quad N_C \geq 12$$

FIG. 9. Energy spectra for intermediate mass fragments of charge $Z = 4$–9 detected in central collisions ($N_C \geq 12$). The curves represent moving source fits [Eq. (2)] with the parameters given in Table III. The distributions represent conditional probability distributions per unit energy and solid angle.

Multiplicity gated energy spectra and angular distributions provide clear evidence for significant nonequilibrium IMF emission, even in central collisions selected by large charged-particle multiplicities. To better characterize the multifragment final state and distinguish between different theoretical scenarios, knowledge of the IMF emission time scale is necessary.

IV. TWO FRAGMENT CORRELATION FUNCTIONS

In this section two-fragment correlation functions are investigated to extract time scales for the emission of intermediate mass fragments. These investigations are conducted at forward angles $16° \leq \theta_{\mathrm{lab}} \leq 31°$, where the statistics of the experimental data and the granularity of the array are optimal for extracting good-quality correlation functions. In Sec. IV A the theoretical models for calculating correlation functions are introduced and the con-

struction of "mixed-fragment" correlation functions is motivated which include sums over different combinations of fragment pairs. In Sec. IV B some of the expected properties of experimental mixed-fragment correlation functions are illustrated. In Sec. IV C the dependence of measured correlation functions upon charged-particle multiplicity and fragment momentum is investigated and compared to simple model calculations.

A. Model calculations

The two-fragment correlation function $1 + R\,(\mathbf{P}, \mathbf{q})$ is defined theoretically by the expression:

$$\sigma_{1,2}(\mathbf{p}_1, \mathbf{p}_2) = C[1 + R\,(\mathbf{P}, \mathbf{q})]\sigma_1(\mathbf{p}_1)\sigma_2(\mathbf{p}_2) , \qquad (5)$$

where $\mathbf{P} = \mathbf{p}_1 + \mathbf{p}_2$, $\mathbf{q} = \mu(\mathbf{p}_1/m_1 - \mathbf{p}_2/m_2) = \mu\mathbf{v}_{\mathrm{rel}}$, and μ are the total momentum, relative momentum, and reduced mass, which are quantities constructed from the individual momenta $\mathbf{p}_1$ and $\mathbf{p}_2$ and individual masses m_1 and m_2 of fragments 1 and 2, respectively. The normalization constant C is determined by the requirement that $\langle R(\mathbf{P}, \mathbf{q}) \rangle = 0$ for values of q sufficiently large that the final-state interaction between the emitted fragments can be neglected.

A particularly simple expression for two-fragment correlation functions integrated over relative orientations between $\mathbf{P}$ and $\mathbf{q}$ can be derived by taking a classical approximation to the Koonin-Pratt formula [72]:

$$1 + R\,(\mathbf{P}, \mathbf{q}) = \int d^3 r_0 F_{\mathbf{P}}(\mathbf{r}_0)(1 - 2\mu\kappa/q^2 r_0)^{1/2} . \qquad (6)$$

Here

TABLE III. Parameters of two-source fits [Eq. (3), using $n = 2$] to fragment spectra observed in central collisions ($N_C \geq 12$). The normalization constants N_i are given in units of $10^{-4}/\mathrm{sr}\,\mathrm{MeV}^{3/2}$.

Z	N_1	v_1/c	T_1 (MeV)	N_2	v_2/c	T_2 (MeV)
4	1.195	0.111	13.8	1.333	0.035	11.4
5	1.306	0.109	13.3	1.226	0.035	11.4
6	1.207	0.096	13.6	0.923	0.035	12.6
7	0.900	0.085	13.3	0.591	0.035	10.1
8	0.620	0.077	13.2	0.533	0.035	9.1
9	0.437	0.077	13.6	0.276	0.035	10.7

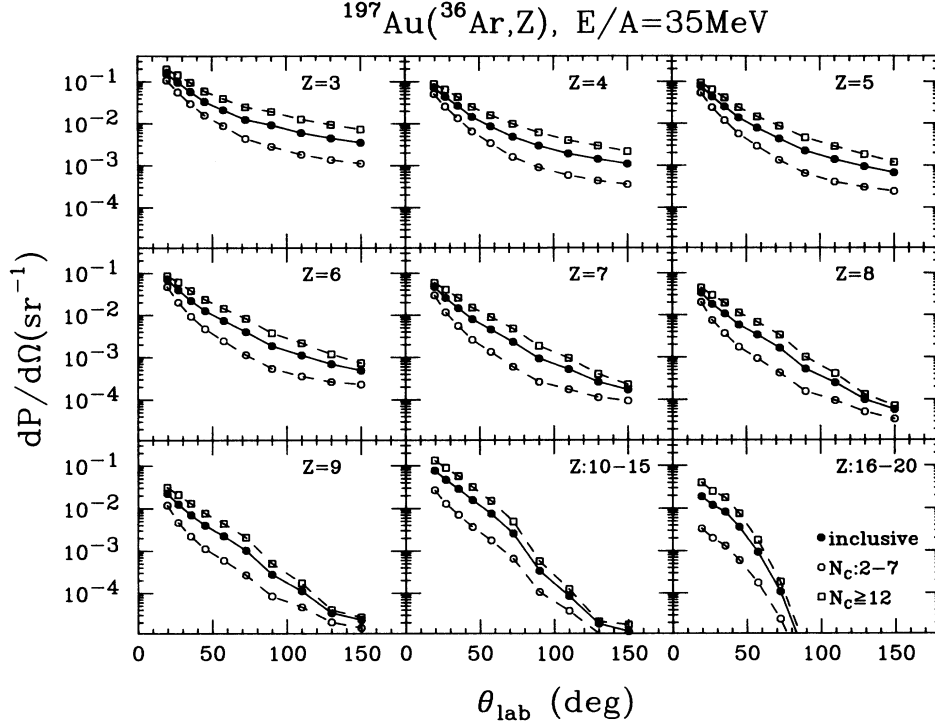$$^{197}\mathrm{Au}(^{36}\mathrm{Ar},Z), \ \ E/A=35\mathrm{MeV}$$

FIG. 10. Comparison of IMF angular distributions measured inclusively (solid points), in central collisions ($N_C \geq 12$, open squares), and in peripheral collisions ($2 \leq N_C \leq 7$, open circles). Different panels show distributions for the indicated fragment Z. The distributions represent normalized conditional probability distributions for collisions preselected by the indicated gates on N_C.

$$F_{\mathbf{P}}(\mathbf{r}) = \frac{\int d^3X \, f_1(\mathbf{P}\mu/m_2, \mathbf{X}+\mathbf{r}\mu/m_1, t_>) f_2(\mathbf{P}\mu/m_1, \mathbf{X}-\mathbf{r}\mu/m_2, t_>)}{|\int d^3X_1 f_1(\mathbf{P}\mu/m_2, \mathbf{X}_1, t_>) \int d^3X_2 f_2(\mathbf{P}\mu/m_1, \mathbf{X}_2, t_>)|} \tag{7}$$

and

$$f_i(\mathbf{p}_i, \mathbf{r}_i, t_>) = \int_{-\infty}^{t_>} dt \, g_i[\mathbf{p}_i, \mathbf{r}_i - \mathbf{p}_i(t_> - t)/m_i, t] \ , \tag{8}$$

where $\kappa = Z_1 Z_2 e^2$ is the product of the charges of the two emitted fragments, $\mathbf{X}$ is the coordinate of the center of mass of the fragment pair, $f_i(\mathbf{p}_i, \mathbf{r}_i, t_>)$ is the phase-space distribution of particles of type i with momentum $\mathbf{p}_i$ at position $\mathbf{r}_i$ at some time $t_>$ after the emission process, and $g_i(\mathbf{p}_i, \mathbf{r}_i, t)$ describes the positions and momenta of the fragments at the point of emission. For a fixed phase-space distribution $F_{\mathbf{P}}(\mathbf{r}_0)$, Eq. (6) depends primarily on the variable

$$v_{\mathrm{red}} = q/\sqrt{\mu\kappa} = v_{\mathrm{rel}}\sqrt{\mu/\kappa} \propto v_{\mathrm{rel}}/\sqrt{Z_1 + Z_2} \ . \tag{9}$$

(In the last step, we have approximated m_i by $2Z_i$.) Thus, according to Eq. (9), one might expect all of the different fragment-fragment correlations to display a similar dependence on v_{red}.

The emission function $g(\mathbf{p}, \mathbf{r}, t)$, was approximated by assuming surface emission from a spherical source of radius R_S with a fixed lifetime τ and energy and angular distribution $dN/dE \, d\Omega$:

$$g(\mathbf{p}, \mathbf{r}, t) \propto (\hat{\mathbf{r}} \cdot \hat{\mathbf{p}}) \Theta(\hat{\mathbf{r}} \cdot \hat{\mathbf{p}}) \delta(r - R_S) \frac{d^2N}{dE \, d\Omega} e^{-t/\tau} \ . \tag{10}$$
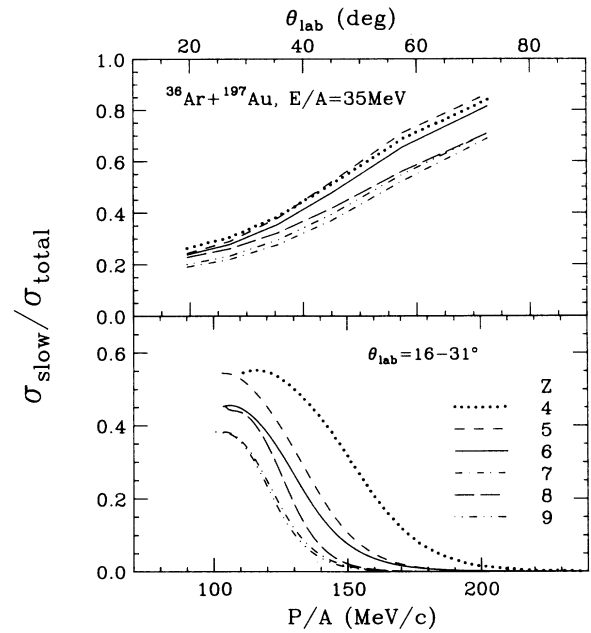

FIG. 11. Equilibrium fraction $\sigma_{\mathrm{slow}}/\sigma_{\mathrm{total}}$ extracted from the fit the data in Fig. 9. Top panel: dependence of energy integrated yield on laboratory angle; bottom panel: dependence on P/A, the momentum per nucleon, of fragments detected at $16° \leq \theta_{\mathrm{lab}} \leq 31°$.

Here $\Theta(x)$ is the unit step function which vanishes for $x < 0$, $\delta(x)$ is the delta function, $\hat{r}$ and $\hat{p}$ are unit vectors parallel to r and p, and $E = p^2/2m$. The energy and angular distributions were taken to be consistent with the experimental distributions. The emitting source was assumed to move with a velocity of $v_S = 0.035c$, consistent with emission from the surface of heavy reaction residues formed in incomplete fusion reactions in which 80% of the projectile momentum was transferred to the fusion-like residue. For the emission of the second fragment, we required a minimum initial separation of $r_{min} = 1.2(A_1^{1/3} + A_2^{1/3})$ fm from the first fragment. In all calculations we assumed a fixed source radius of $R_S = 12$ fm. Choosing a smaller source radius leads to more significant Coulomb final-state interactions; this, to first order, has the same effect on the correlation function as reducing the emission time scale. Likewise, an increase in the source radius cannot be easily distinguished from an increase in the emission time scale.

Sensitivities to reasonable variations in the parameters describing $g(p,r,t)$ were discussed in Ref. [71]; they typically introduce uncertainties of the order of 50% of the extracted emission times. To determine more accurate emission time scales would require more realistic emission functions and source charge distributions. Such information would also allow more accurate calculations that avoid some of the model assumptions incorporated in the Koonin-Pratt formalism. For example, Eqs. (6)–(9) were obtained by assuming that final-state interactions between the two detected particles are so dominant that interactions with the remaining particles can be neglected. The specific form of Eq. (6) also reflects the additional assumption that the single-fragment phase-space distributions vary only slowly over the individual particle momenta. As discussed in Ref. [72], both assumptions may not be satisfied for realistic IMF emission functions.

In order to evaluate some of the theoretical uncertainties associated with these model assumptions, we have also performed classical trajectory calculations and constructed theoretical correlation functions according to Eq. (5) [or, equivalently, Eq. (11) below]. The initial positions and momenta of the two detected fragments were determined from Eq. (10). Coulomb distortions due to the interaction of the two emitted fragments with a heavy fusionlike residue were modeled by three-body Coulomb trajectory calculations assuming a heavy residue of initial charge number $Z_S = 79$. To establish the magnitude of these three-body Coulomb distortions, trajectory calculations were also performed with the Coulomb interaction with the heavy residue eliminated; these calculations are designated by the notation $Z_S = 0$. Recoil effects were incorporated by assuming the residue has a mass of $A_S = 197u$. In all trajectory calculations, the response of the experimental apparatus was taken into account.

Finally, it should be noted that our schematic model calculations do not address the possible existence of dynamical correlations between the positions and momenta of the fragments which go beyond our present parametrization of the emission function. The description of such effects, if important, requires a better microscopic understanding of the fragment emission mechanism than is currently available. Such questions lie beyond the scope of the present investigation.

B. Combinations of different fragment pairs

The experimental correlation function $1 + R$ is constructed from the measured coincidence and single-particle yields $Y_{12}(p_1,p_2)$ and $Y_i(p_i)$, respectively, according to the expression

$$\sum Y_{12}(p_1,p_2) = C[1 + R(\zeta)] \sum Y_1(p_1)Y_2(p_2) , \quad (11)$$

where $\zeta = q$ or v_{red}. The normalization constant C is determined by the requirement that $\langle R(\zeta) \rangle = 0$ for values of ζ sufficiently large that the final-state interaction between the emitted fragments can be neglected. For each gating condition (on P and/or other quantities), the correlation function is evaluated by summing both sides of Eq. (5) over all momentum combinations corresponding to given values of ζ. Since the yields differ from the cross sections only by overall normalization constants, Eq. (11) is equivalent to Eq. (5).

In Fig. 12 we compare correlation functions for representative pairs of intermediate mass fragments alternatively as functions of relative momentum q (top panel) or as a function of reduced relative velocity v_{red} (bottom panel). Different symbols in the figure denote correlation functions evaluated for different fragment pairs ($Z_1 = 6$ and $4 \leq Z_2 \leq 9$). Since the Coulomb repulsion is greater between fragments of greater charge, the correlation functions $1 + R(q)$ exhibit wider minima at $q \approx 0$ for increased charge of the second fragment. When plotted as
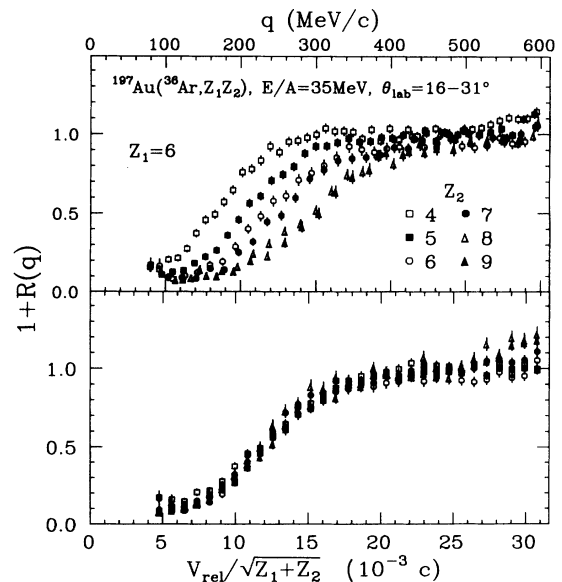

FIG. 12. Dependence of inclusive, energy-integrated two-fragment correlation functions on relative momentum q (top panel) and on reduced relative velocity $v_{rel}/\sqrt{Z_1 + Z_2}$. One fragment was carbon ($Z = 6$); the atomic number Z_2 of the other fragment is indicated.

a function of v_{red}, however, the correlation functions $1+R(v_{red})$ are very similar. This suggests that correlation functions may be summed over different pair combinations and evaluated as a function of the reduced relative velocity with little loss in resolution. This "mixed-fragment" analysis permits the exploration of emission time scales with significantly improved statistical precision. In the following we construct mixed-fragment correlation functions according to Eq. (11), where the sum is extended over all charge combinations with $4 \leq Z_1, Z_2 \leq 9$. Sufficient statistics are achieved via this summation to allow the exploration of emission time scales as functions of the charged-particle multiplicity and velocity of the emitted fragments.

Our definition of the mixed-fragment correlation function differs slightly from that adopted in Ref. [56], where two-fragment correlation functions were evaluated as a function of the relative fragment velocity. Figure 13 illustrates the difference between the two prescriptions. The top and bottom panels of the figure show correlation functions evaluated, for different fragment combinations with $4 \leq Z_1, Z_2 \leq 9$, as functions of relative and reduced relative velocities v_{rel} and $v_{rel}/\sqrt{Z_1+Z_2}$, respectively. For this range of fragment charges, mixed-fragment correlation functions display superior resolution when they are evaluated as a function of the reduced relative velocity. Of course, the loss of resolution incurred for $1+R(v_{rel})$ can be incorporated into the model calculations by performing corresponding averages [56].

C. Gated correlation functions

Measured energy-integrated two-fragment correlation functions, gated by various conditions on charged-

particle and intermediate mass fragment multiplicities, are shown in Fig. 14. The top and bottom panels show correlation functions gated by various conditions on charged-particle and IMF multiplicity, N_C and N_{IMF}, respectively. For orientation, we include calculations with the Koonin-Pratt formula [71,72] for different emission times τ. Correlation functions measured for peripheral collisions or for events in which only two intermediate mass fragments were detected exhibit considerable distortions at larger reduced relative velocities. Since these distortions are not yet understood, they introduce slight uncertainties in the asymptotic normalization of the correlation functions. They become less significant for central collisions or for events in which at least four fragments are detected. The shapes of the energy-integrated correlation functions depend only slightly on these multiplicity gates. The width of the minimum at $v_{red} \approx 0$ appears to decrease slightly as more central collisions (larger charged-particle multiplicities) are selected. This observation is qualitatively consistent with slightly longer time scales (or larger source dimensions) for fragments emitted in central as compared to peripheral collisions.

Figure 15 depicts two-fragment correlation functions gated by central collisions ($N_C \geq 12$). In order to be able to study fragment emission time scales for different regions of the kinetic-energy spectrum, we have evaluated the correlation functions for three different ranges of $P/A = |\mathbf{p}_1+\mathbf{p}_2|/(A_1+A_2)$, the total momentum per nucleon of the coincident fragment pair. The low-momentum gate ($P/A \leq 110$ MeV/c, solid circular points) selects fragment kinetic energies at and below the exit channel Coulomb barrier. Kinetic energies slightly above the Coulomb barrier are selected by the
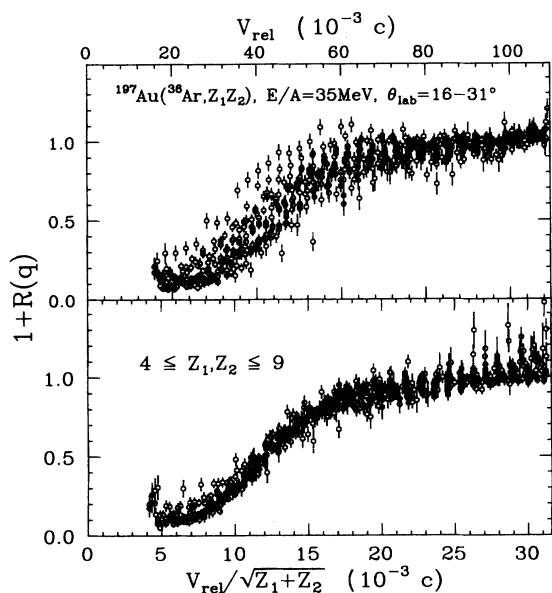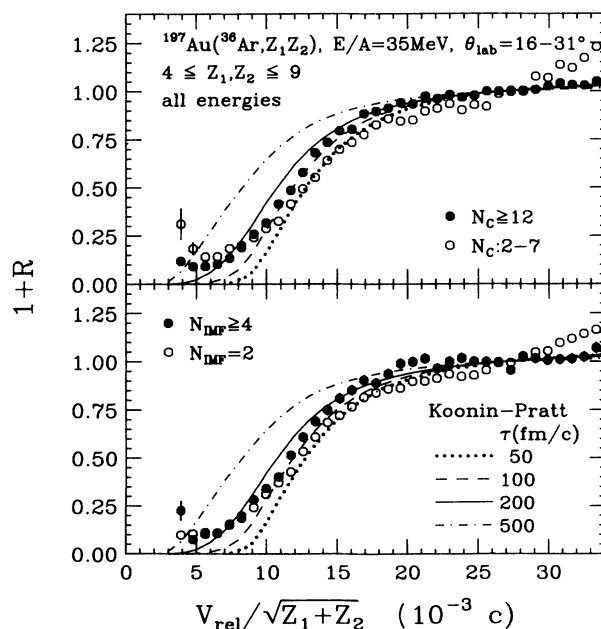

FIG. 13. Dependence of inclusive, energy-integrated two-fragment correlation functions on relative velocity v_{rel} (top panel) and on reduced relative velocity $v_{rel}/\sqrt{Z_1+Z_2}$ (bottom panel). Two-fragment correlation functions are shown for each combination of Z_1 and Z_2, with $4 \leq Z_1, Z_2 \leq 9$.

FIG. 14. Two-fragment correlation functions summed over all combinations of Z_1 and Z_2 (with $4 \leq Z_1, Z_2 \leq 9$) and selected by the indicated gates on charged-particle multiplicity N_C (top panel) and on IMF multiplicity N_{IMF} (bottom panel).
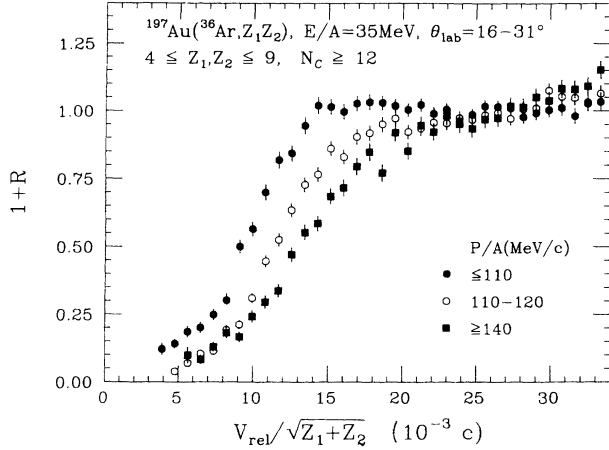
FIG. 15. Two-fragment correlation functions summed over all combinations of Z_1 and Z_2 (with $4 \leq Z_1, Z_2 \leq 9$) and selected by central collisions ($N_C \geq 12$). The correlation functions are evaluated for the indicated ranges of P/A, the total momentum per nucleon of the detected fragment pair.

FIG. 16. Inclusive, energy-integrated two-fragment correlation functions summed over all combinations of Z_1 and Z_2 (with $4 \leq Z_1, Z_2 \leq 9$). The different panels give comparisons with different calculations discussed in the text.

intermediate-momentum gate ($P/A = 110-120$ MeV/c, open circular points). For these two gates, a considerable part of the emission cross section is consistent with equilibrium emission (see also Fig. 11). Kinetic energies significantly above the Coulomb barrier are selected by the high-momentum gate ($P/A \geq 140$ MeV/c, solid square-shaped points). In this domain fragment emission for central collisions is dominated by nonequilibrium emission processes different from projectile fragmentation. The experimental correlation functions exhibit a rather pronounced dependence on the total momentum per nucleon of the emitted fragment pairs. The minimum at $v_{\mathrm{red}} \approx 0$ becomes considerably wider as the gate on P/A is raised from below 110 MeV/c to above 140 MeV/c. Since wider minima are indicative of smaller space-time dimensions [71,72], this observation is qualitatively consistent with the expectation that mean emission times should become shorter as the kinetic energy of the emitted fragment is raised from close to the Coulomb barrier to much higher values.

In Fig. 16 the measured inclusive two-fragment correlation functions are compared to correlation functions calculated for the indicated emission times τ. Calculations with the Koonin-Pratt formula [Eq. (6)] are presented in the top panel; the center and bottom panels show the results of numerical trajectory calculations for $Z_S = 0$ and 79, respectively. Calculations neglecting Coulomb interactions with the residual system (upper and center panels) predict shapes of correlation functions which are in slightly better agreement with the experimental correlation functions than the three-body calculations incorporating distortions in the field of a heavy reaction residue (bottom panel). Slightly smaller emission times are indicated by calculations with the Koonin-Pratt formula and by the $Z_S = 0$ calculations than by the three-charged-body calculations. Nevertheless, all calculations are consistent with emission times between $\tau = 100$ and 200 fm/c, in agreement with the results from our previ-
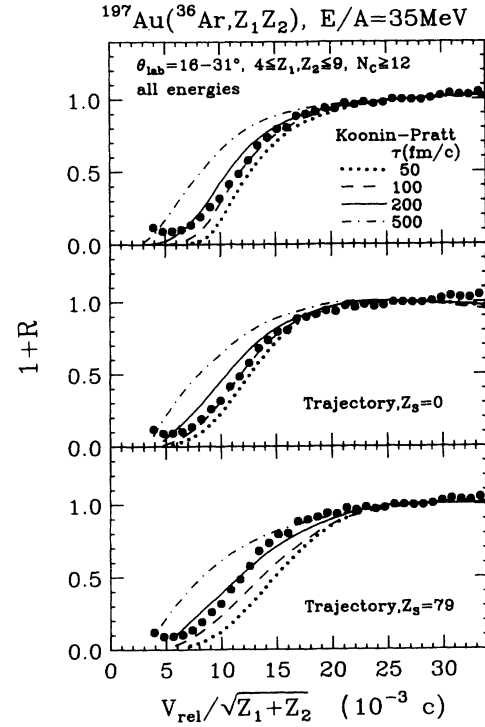
ous analysis [71] of Be-Be, B-B, and C-C correlation functions.

Calculations for correlation functions measured for central collisions and for different cuts on P/A, the total momenta per nucleon of the coincident fragments pairs, are presented in Figs. 17–19. Individual panels of these figures depict results for the indicated cuts on P/A. Figures 17, 18, and 19 present calculations for different emission times using the Koonin-Pratt formula and trajectory calculations for $Z_S = 0$ and 79, respectively. For the case $Z_S = 79$, three-body trajectory calculations could only be performed for the two higher-momentum cuts, $P/A = 110-120$ MeV/c and $P/A \geq 140$ MeV/c, as the cut $P/A \leq 110$ MeV/c selects mostly energies below the Coulomb barrier. For clarity and consistency, we refrained from lowering the exit channel Coulomb barrier which would require a significant increase in source radius or a significant decrease of the source charge. Either of these parameter modifications would reduce Coulomb distortions and, hence, differences with the Koonin-Pratt and $Z_S = 0$ calculations.

For all three approximations investigated, comparisons between theoretical and experimental correlation functions lead to qualitatively similar conclusions: The emission of energetic fragments is governed by significantly smaller time scales than the emission of low-energy fragments with energies close to the exit channel Coulomb barrier. Such a dependence is consistent with the

predominance of nonequilibrium emission processes for energetic fragment emissions and the increasing importance of emission from more equilibrated systems for particles emitted with energies close to the Coulomb barrier (see also Fig. 11). As was already observed for the inclusive correlation functions, calculations with the Koonin-Pratt formula and those for $Z_S = 0$ predict shapes of correlation functions which are in better agreement with the experimental data than those predicted by three-body trajectory calculations. These former calculations indicate emission times of $\tau \lesssim 50$ fm/c for the emission of energetic fragments selected by $P/A \geq 140$ MeV/c and considerably larger emission times $\tau \approx 500$ fm/c for subbarrier emission selected by $P/A \leq 110$ MeV/c. Emission times extracted for $P/A = 110-120$ MeV/c are of the order of $\tau \approx 150$ fm/c. Qualitatively similar conclusions are drawn from a comparison with the three-body trajectory calculations for $Z_S = 79$.

Emission time scales of the order of several hundred fm/c are consistent with time scales expected from statistical models of compound nuclear decays. For example, the model of Ref. [40] predicts average time intervals of $\tau \approx 300$ fm/c between the emission of two carbon fragments from equilibrated heavy nuclei ($A = 226$, $Z = 93$) of 700 MeV excitation energy. Much shorter time scales

$\tau \approx 50-100$ fm/c, extracted for the emission of energetic fragments in central collisions, are incompatible with statistical emission from fully equilibrated heavy reaction residues. These emission times are of comparable magnitude as those predicted [10–13] by dynamical models of fragment production.

V. SUMMARY AND CONCLUSION

We have studied the emission of intermediate mass fragments in collisions between ^{36}Ar projectiles and ^{197}Au target nuclei at $E/A = 35$ MeV. The measurements were performed with a low-threshold charged-particle detector array covering the polar angles of $16° \leq \theta_{lab} \leq 160°$ and subtending a solid angle of 85% of 4π.

Intermediate mass fragments are preferentially emitted in violent central collisions characterized by large charged-particle multiplicities N_C. In peripheral collisions fragment emission is a fairly unlikely process; the average IMF multiplicity increases from $\langle N_{IMF} \rangle \lesssim 0.1$ for $N_C = 2$ to $\langle N_{IMF} \rangle \approx 1.2$ for $N_C \gtrsim 15$. The elemental distributions observed for various cuts on charged-particle multiplicity exhibit a nearly exponential falloff as a function of Z. In this reaction the inclusive element distributions are rather similar to those observed in cen-
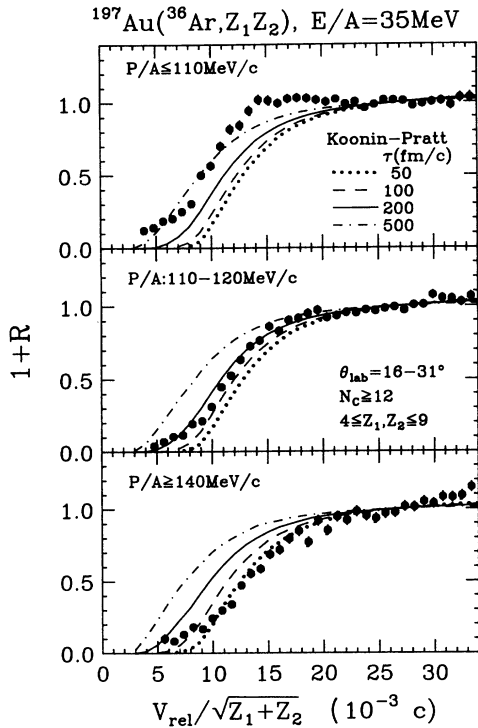

FIG. 17. Two-fragment correlation functions summed over all combinations of Z_1 and Z_2 (with $4 \leq Z_1, Z_2 \leq 9$) and selected by central collisions ($N_C \geq 12$). Individual panels show the correlation functions for the indicated cuts on P/A, the total momentum per nucleon of the detected fragment pair. The curves represent calculations with the Koonin-Pratt formula for the indicated emission times.
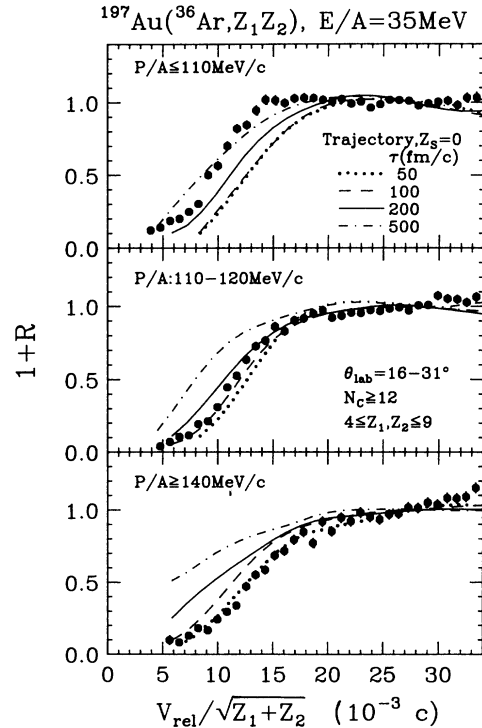
FIG. 18. Two-fragment correlation functions summed over all combinations of Z_1 and Z_2 (with $4 \leq Z_1, Z_2 \leq 9$) and selected by central collisions ($N_C \geq 12$). Individual panels show the correlation functions for the indicated cuts on P/A, the total momentum per nucleon of the detected fragment pair. The curves represent the results of trajectory calculations for which the Coulomb interaction with the residual system is turned off. The key for emission times is given in the figure.
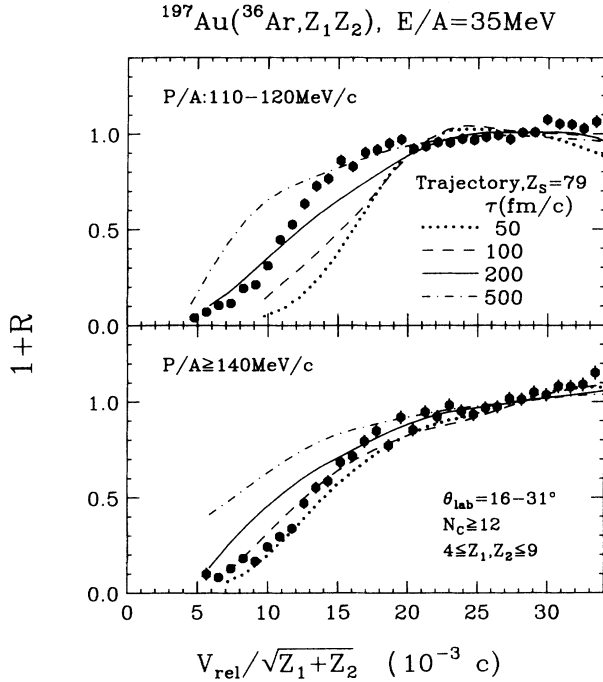
^{197}Au(^{36}Ar,Z_1Z_2), E/A=35MeV

FIG. 19. Two-fragment correlation functions summed over all combinations of Z_1 and Z_2 (with $4 \leq Z_1, Z_2 \leq 9$) and selected by central collisions ($N_C \geq 12$). Individual panels show the correlation functions for the indicated cuts on P/A, the total momentum per nucleon of the detected fragment pair. The curves represent the results of three-body Coulomb trajectory calculations in which the two fragments are assumed to be emitted from a source of initial charge number $Z_S = 79$. The key for emission times is given in the figure.

tral collisions. The exponential falloff is only slightly steeper for fragments produced in peripheral collisions than for fragments produced in central collisions. The angular distributions of fragments produced in peripheral collisions are steeper than those of fragments produced in central collisions. At forward angles the energy spectra of fragments produced in peripheral collisions exhibit a high-energy shoulder, which could be attributed to emission from a projectilelike source. Such a shoulder is not observed in energy spectra gated on central collisions, for which the spectra exhibit nearly exponential shapes.

A detailed analysis of the energy and angular distributions of fragments emitted in central collisions (gated by $N_C \geq 12$) reveals important contributions from processes incompatible with emission from equilibrated sources. These contributions dominate for fragments emitted at forward angles and with kinetic energies well above the exit channel Coulomb barrier. Emission with kinetic energies close to the Coulomb barrier and at larger angles is consistent with increasing contributions from the decay of equilibrated heavy reaction residues.

The granularity of the apparatus and the statistics of two-fragment coincidences allowed the generation of good-quality two-fragment correlation functions in the angular range of $16° \leq \theta_{lab} \leq 31°$. As suggested in Ref. [72], the two-fragment correlation function was found to

depend mainly on the reduced relative velocity of the fragment pairs. This scaling allows the construction of mixed-fragment correlation functions with little loss in resolution and significantly improved statistics, thus allowing a detailed investigation of two-fragment correlation functions for different multiplicity cuts and different ranges of fragment velocities.

Average emission time scales of $\tau = 100-200$ fm/c were extracted from the inclusive, mixed-fragment correlation functions. These values are consistent with the emission times extracted from Be-Be, B-B, and C-C correlation functions [71]. Only modest dependences were observed for various cuts on charged-particle or IMF multiplicity. These dependences were qualitatively consistent with slightly larger space-time dimensions for central than for peripheral collisions.

In order to suppress contributions from the decay of projectilelike residues, we constructed two-fragment correlation functions for central collisions (gated by $N_C \geq 12$). We explored various cuts on P/A, the total momentum per nucleon of the emitted fragment pair, which select different ranges of fragment velocities and, hence, different relative contributions from equilibrium and nonequilibrium emission. The observed dependence on P/A indicated significant differences in emission time scales. In order to extract fragment emission times, we assumed, for simplicity, emission from the surface of a spherical source of 12 fm radius. For the most energetic fragments, the correlation functions were consistent with mean emission times of $\tau < 100$ fm/c, possibly as short as $\tau \approx 50$ fm/c. For fragments emitted with kinetic energies at or below the exit channel Coulomb barrier, the correlation functions indicate much longer emission time scales $\tau \gtrsim 300$ fm/c, possibly as large as $\tau \approx 500$ fm/c. For comparison, average emission times predicted for the decay of equilibrated fusion residues are of the order of 300 fm/c; dynamical models of fragment production predict emission time scales on the order of 50 fm/c.

The shape of the fragment energy spectra and emission time scales extracted from two-fragment correlation functions indicates that fragment emission in central collisions begins at the very early stages of the reaction and continues throughout the later equilibrated stages. Thus realistic models of fragment production must strive to describe the competition between light-particle and IMF emission from the early, possibly compressed stages of the reaction, to the later, equilibrated, and possibly expanded stages.

ACKNOWLEDGMENTS

[1] G. Bertsch and P. J. Siemens, Phys. Lett. **126B**, 9 (1983).

[2] H. Sagawa and G. F. Bertsch, Phys. Lett. **155B**, 11 (1985).

[3] H. Schulz, D. N. Voskresensky, and J. Bondorf, Phys. Lett. **147B**, 17 (1984).

[4] S. Levit and P. Bonche, Nucl. Phys. **A437**, 426 (1984).

[5] A. Vicentini, G. Jacucci, and V. R. Pandharipande, Phys. Rev. C **31**, 1783 (1985).

[6] R. J. Lenk and V. R. Pandharipande, Phys. Rev. C **34**, 177 (1986).

[7] T. J. Schlagel and V. R. Pandharipande, Phys. Rev. C **36**, 162 (1987).

[8] W. Bauer, G. F. Bertsch, and S. Das Gupta, Phys. Rev. Lett. **58**, 863 (1987).

[9] K. Sneppen and L. Vinet, Nucl. Phys. **A480**, 342 (1988).

[10] J. Aichelin, G. Peilert, A. Bohnet, A. Rosenhauer, H. Stöcker, and W. Greiner, Nucl. Phys. **A488**, 437c (1988).

[11] J. Aichelin, G. Peilert, A. Bohnet, A. Rosenhauer, H. Stöcker, and W. Greiner, Phys. Rev. C **37**, 2451 (1988).

[12] G. Peilert, H. Stöcker, W. Greiner, A. Rosenhauer, A. Bohnet, and J. Aichelin, Phys. Rev. C **39**, 1402 (1989).

[13] D. H. Boal and J. N. Glosli, Phys. Rev. C **37**, 91 (1988).

[14] E. Suraud, Nucl. Phys. **A495**, 73 (1989).

[15] X. Campi, Phys. Lett. B **208**, 351 (1988).

[16] W. Bauer, Phys. Rev. C **38**, 1297 (1988).

[17] C. Ngô, H. Ngô, S. Leray, and M. E. Spina, Nucl. Phys. **A499**, 148 (1989).

[18] D. H. Boal and J. Glosli, Phys. Rev. C **42**, 502 (1990).

[19] J. Randrup and S. Koonin, Nucl. Phys. **A356**, 223 (1981).

[20] G. Fai and J. Randrup, Nucl. Phys. **A381**, 557 (1982).

[21] G. Fai and J. Randrup, Phys. Lett. **115B**, 281 (1982).

[22] G. Fai and J. Randrup, Nucl. Phys. **A404**, 281 (1983).

[23] D. H. E. Gross, L. Satpathy, T. C. Meng, and M. Satpathy, Z. Phys. **A309**, 41 (1982).

[24] D. H. E. Gross and X. Z. Zhang, Phys. Lett. **161B**, 47 (1985).

[25] Sa Ban-Hao and D. H. E. Gross, Nucl. Phys. **A437**, 643 (1985).

[26] D. H. E. Gross, X. Z. Zhang, and S. Y. Xu, Phys. Rev. Lett. **56**, 1544 (1986).

[27] X. Z. Zhang, D. H. E. Gross, S. Y. Xu, and Y. M. Zheng, Nucl. Phys. **A461**, 641 (1987).

[28] X. Z. Zhang, D. H. E. Gross, S. Y. Xu, and Y. M. Zheng, Nucl. Phys. **A461**, 668 (1987).

[29] D. H. E. Gross, Phys. Lett. B **203**, 26 (1988).

[30] J. P. Bondorf, R. Donangelo, I. N. Mishustin, C. J. Pethick, H. Schulz, and K. Sneppen, Nucl. Phys. **A443**, 321 (1985).

[31] J. P. Bondorf, R. Donangelo, I. N. Mishustin, and H. Schulz, Nucl. Phys. **A444**, 460 (1985).

[32] J. P. Bondorf, R. Donangelo, I. N. Mishustin, C. J. Pethick, and K. Sneppen, Phys. Lett. **150B**, 57 (1985).

[33] J. P. Bondorf, R. Donangelo, H. Schulz, and K. Sneppen, Phys. Lett. **162B**, 30 (1985).

[34] R. Donangelo, K. Sneppen, and J. P. Bondorf, Phys. Lett. **219B**, 165 (1989).

[35] L. G. Moretto, Nucl. Phys. **A247**, 211 (1975).

[36] W. A. Friedman and W. G. Lynch, Phys. Rev. C **28**, 950 (1983).

[37] L. G. Moretto and G. Wozniak, Prog. Part. Nucl. Phys. **38**, 401 (1988).

[38] W. A. Friedman, Phys. Rev. Lett. **60**, 2125 (1988).

[39] W. A. Friedman, Phys. Rev. C **40**, 2055 (1989).

[40] W. A. Friedman, Phys. Rev. C **42**, 667 (1990).

[41] C. Barbagallo, J. Richert, and P. Wagner, Z. Phys. A **324**, 97 (1986).

[42] J. Richert and P. Wagner, Nucl. Phys. **A517**, 399 (1990).

[43] W. Lynch, Annu. Rev. Nucl. Part. Sci. **37**, 493 (1987), and references contained therein.

[44] J. E. Finn, S. Agarwal, A. Bujak, J. Chuang, L. J. Gutay, A. S. Hirsch, R. W. Minich, N. T. Porile, R. P. Scharenberg, B. C. Stringfellow, and F. Turkot, Phys. Rev. Lett. **49**, 1321 (1982).

[45] A. S. Hirsch, A. Bujak, J. E. Finn, L. J. Gutay, R. W. Minich, N. T. Porile, R. P. Scharenberg, B. C. Stringfellow, and F. Turkot, Phys. Rev. C **29**, 508 (1984).

[46] A. D. Panagiotou, M. W. Curtin, H. Toki, D. K. Scott, and P. J. Siemens, Phys. Rev. Lett. **52**, 496 (1984).

[47] C. B. Chitwood, D. J. Fields, C. K. Gelbke, W. G. Lynch, A. D. Panagiotou, M. B. Tsang, H. Utsunomiya, and W. A. Friedman, Phys. Lett. **131B**, 289 (1983).

[48] L. G. Sobotka, M. A. McMahan, R. J. McDonald, C. Signarbieux, G. J. Wozniak, M. L. Padgett, J. H. Gu, Z. H. Liu, Z. Q. Yao, and L. G. Moretto, Phys. Rev. Lett. **53**, 2004 (1984).

[49] D. J. Fields, W. G. Lynch, C. B. Chitwood, C. K. Gelbke, M. B. Tsang, H. Utsunomiya, and J. Aichelin, Phys. Rev. C **30**, 1912 (1984).

[50] D. J. Fields, W. G. Lynch, T. K. Nayak, M. B. Tsang, C. B. Chitwood, C. K. Gelbke, R. Morse, J. Wilczynski, T. C. Awes, R. L. Ferguson, F. Plasil, F. E. Obenshain, and G. R. Young, Phys. Rev. C **34**, 536 (1986).

[51] B. V. Jacak, G. D. Westfall, G. M. Crawley, D. Fox, C. K. Gelbke, L. H. Harwood, B. E. Hasselquist, W. G. Lynch, D. K. Scott, H. Stöcker, M. B. Tsang, G. Buchwald, and T. J. M. Symons, Phys. Rev. C **35**, 1751 (1987).

[52] D. E. Fields, K. Kwiatkowski, D. Bonser, R. W. Viola, V. E. Viola, W. G. Lynch, J. Pochodzalla, M. B. Tsang, C. K. Gelbke, D. J. Fields, and S. M. Austin, Phys. Lett. B **220**, 356 (1989).

[53] J. W. Harris, B. V. Jacak, K. H. Kampert, G. Claesson, K. G. R. Doss, R. Ferguson, A. I. Gavron, H. A. Gustafsson, H. Gutbrod, B. Kolb, F. Lefebvres, A. M. Poskanzer, H. G. Ritter, H. R. Schmidt, L. Teitelbaum, M. Tincknell, S. Weiss, H. Wieman, and J. Wilhelmy, Nucl. Phys. **A471**, 241c (1987).

[54] K. G. R. Doss, H. A. Gustafsson, H. Gutbrod, J. W. Harris, B. V. Jacak, K. H. Kampert, A. M. Poskanzer, H. G. Ritter, H. R. Schmidt, L. Teitelbaum, M. Tincknell, S. Weiss, and H. Wieman, Phys. Rev. Lett. **59**, 2720 (1987).

[55] D. R. Bowman, W. L. Kehoe, R. J. Charity, M. A. McMahan, A. Moroni, A. Bracco, S. Bradley, I. Iori, R. J. McDonald, A. C. Mignerey, L. G. Moretto, M. N. Namboodiri, and G. J. Wozniak, Phys. Lett. B **189**, 282 (1987).

[56] R. Trockel, U. Lynen, J. Pochodzalla, W. Trautmann, N. Brummund, E. Eckert, R. Glasow, K. D. Hildenbrand, K. H. Kampert, W. F. W. Müller, D. Pelte, H. J. Rabe, H. Sann, R. Santo, H. Stelzer, and R. Wada, Phys. Rev. Lett. **59**, 2844 (1987).

[57] Y. D. Kim, M. B. Tsang, C. K. Gelbke, W. G. Lynch, N. Carlin, Z. Chen, R. Fox, W. G. Gong, T. Murakami, T. K. Nayak, R. M. Ronningen, H. M. Xu, F. Zhu, W. Bauer, L. G. Sobotka, D. Stracener, D. G. Sarantites, Z. Majka, V. Abenante, and H. Griffin, Phys. Rev. Lett. **63**, 494 (1989).

[58] Y. Blumenfeld, N. Colonna, P. Roussel-Chomaz, D. N. Delis, K. Hanold, J. C. Meng, G. F. Peaslee, G. J. Wozniak, L. G. Moretto, B. Libby, G. Guarino, N. Santoruvo, and I. Iori, Phys. Rev. Lett. **66**, 576 (1991).

[59] For a recent review, see, e.g., D. H. Boal, C. K. Gelbke,

and B. K. Jennings, Rev. Mod. Phys. **62**, 553 (1990).

[60] G. I. Kopylov and M. I. Podgoretskii, Yad. Fiz. **14**, 392 (1972) [Sov. J. Nucl. Phys. **15**, 219 (1972)].

[61] S. E. Koonin, Phys. Lett. **70B**, 43 (1977).

[62] S. Pratt and M. B. Tsang, Phys. Rev. C **36**, 2390 (1987).

[63] W. G. Gong, W. Bauer, C. K. Gelbke, and S. Pratt, Phys. Rev. C **43**, 781 (1991).

[64] P. A. De Young, M. S. Gordon, Xiu qin Lu, R. L. McGrath, J. M. Alexander, D. M. de Castro Rizzo, and L. C. Vaz, Phys. Rev. C **39**, 128 (1989).

[65] P. A. DeYoung, C. J. Gelderloos, D. Kortering, J. Sarafa, K. Zienert, M. S. Gordon, B. J. Fineman, G. P. Gilfoyle, X. Lu, R. L. McGrath, D. M. de Castro Rizzo, J. M. Alexander, G. Auger, S. Kox, L. C. Vaz, C. Beck, D. J. Henderson, D. G. Kovar, and M. F. Vineyard, Phys. Rev. C **41**, R1885 (1990).

[66] J. Québert, R. Boisgard, P. Lautridou, D. Ardouin, D. Durand, D. Goujdami, F. Guilbault, C. Lebrun, R. Tamisier, A. Péghaire, and F. Saint-Laurent, in *Proceedings of the Symposium on Nuclear Dynamics and Nuclear Disassembly, Dallas, April 1989*, edited by J. B. Natowitz (World Scientific, Singapore, 1989), p. 337.

[67] D. Ardouin, F. Guilbault, C. Lebrun, D. Ardouin, S. Pratt, P. Lautridou, R. Boisgard, J. Québert, and A. Péghaire, University of Nantes, Internal Report No. LPN-89-02, 19xx.

[68] W. G. Gong, C. K. Gelbke, N. Carlin, R. T. de Souza, Y. D. Kim, W. G. Lynch, T. Murakami, G. Poggi, D. Sanderson, M. B. Tsang, H. M. Xu, D. E. Fields, K. Kwiatkowski, R. Planeta, V. E. Viola, Jr., S. J. Yennello, and S. Pratt, Phys. Lett. B **246**, 21 (1990).

[69] W. G. Gong, C. K. Gelbke, W. Bauer, N. Carlin, R. T. de Souza, Y. D. Kim, W. G. Lynch, T. Murakami, G. Poggi, D. P. Sanderson, M. B. Tsang, H. M. Xu, D. E. Fields, K. Kwiatkowski, R. Planeta, V. E. Viola, Jr., S. J. Yennello, and S. Pratt, Phys. Rev. C **43**, 1804 (1991).

[70] W. G. Gong, W. Bauer, C. K. Gelbke, N. Carlin, R. T. de Souza, Y. D. Kim, W. G. Lynch, T. Murakami, G. Poggi, D. P. Sanderson, M. B. Tsang, H. M. Xu, S. Pratt, D. E. Fields, K. Kwiatkowski, R. Planeta, V. E. Viola, Jr., and S. J. Yennello, Phys. Rev. Lett. **65**, 2114 (1990).

[71] Y. D. Kim, R. T. de Souza, D. R. Bowman, N. Carlin, C. K. Gelbke, W. G. Gong, W. G. Lynch, L. Phair, M. B. Tsang, F. Zhu, and S. Pratt, Phys. Rev. Lett. **67**, 14 (1991).

[72] Y. D. Kim, R. T. de Souza, C. K. Gelbke, W. G. Gong, and S. Pratt , Phys. Rev. C (in press).

[73] R. T. de Souza, N. Carlin, Y. D. Kim, J. Ottarson, L. Phair, D. R. Bowman, C. K. Gelbke, W. G. Gong, W. G. Lynch, R. A. Pelak, T. Peterson, G. Poggi, M. B. Tsang, and H. M. Xu, Nucl. Instrum. Methods A **295**, 109 (1990).

[74] C. Cavata, M. Demoulins, J. Gosset, M. C. Lemaire, D. L'Hôte, J. Poitou, and O. Valette, Phys. Rev. C **42**, 1760 (1990).

[75] J. L. Wile, D. E. Fields, K. Kwiatkowski, K. B. Morley, E. Renshaw, S. J. Yennello, V. E. Viola, N. Carlin, C. K. Gelbke, W. G. Gong, W. G. Lynch, R. T. de Souza, M. B. Tsang, and H. M. Xu, Phys. Lett. B **264**, 26 (1991).

[76] C. B. Chitwood, D. J. Fields, C. K. Gelbke, D. R. Klesch, W. G. Lynch, M. B. Tsang, T. C. Awes, R. L. Ferguson, F. E. Obenshain, F. Plasil, R. L. Robinson, and G. R. Young, Phys. Rev. C **34**, 858 (1986).

[77] M. Fatyga, K. Kwiatkowski, V. E. Viola, C. B. Chitwood, D. J. Fields, C. K. Gelbke, W. G. Lynch, J. Pochodzalla, M. B. Tsang, and M. Blann, Phys. Rev. Lett. **55**, 1376 (1985).

[78] Y. Cassagnou, M. Conjeaud, R. Dayras, S. Harars, G. Klotz-Engmann, R. Legrain, V. Lips, H. Oeschler, E. C. Pollaco, and C. Volant, in *Proceedings of the Symposium on Nuclear Dynamics and Nuclear Disassembly* (Ref. [66]), p. 386.